Supplementary Information for
Direct measuring of single heterogeneous bubble nucleation
mediated by surface topology

Xiaoli Deng,[a⊥] Yun Shan,[a⊥] Xiaohui Meng,[b] Zhaoyang Yu,[c] Xiaoxi Lu,[a] Yunqing Ma,[c] Jiao Zhao,[a]
Dong Qiu,[b] Xianren Zhang,[c] Yuwen Liu,[d] Qianjin Chen[a]*

Qianjin Chen
Email: qianjinchen@dhu.edu.cn

This PDF file includes:

Supplementary text
Figures S1 to S29
Tables S1 to S3
SI References

Synthesize and SEM characterization of SiO₂ nanoparticles

SiO_2 nanoparticles larger than 5.3 nm were synthesized using the seeded growth, where very small amount of SDS (0.05 mg/mL) was added to reduce the size of TEOS droplet, thus accelerating subsequent TEOS hydrolysis. Importantly, SDS has very weak binding on SiO_2 surface, and was removed using repeated centrifugation after synthesis. The obtained spherical SiO_2 colloids shows highly monodispersed size (Fig. S1). Zeta potential measurement shows the synthesized colloids are neutrally charged in aqueous solution at pH=7.

AFM characterization of bare and particle deposited glassy carbon surface

Fig. S2 shows the high-resolution atomic force microscope (AFM) image of a 5×5 µm² region, where a local root-mean-square roughness of 1.35 nm is revealed. Upon silica nanoparticle deposition, individual isolated nanoparticles (5.3 nm radius for example) are clearly observed, assuring subsequent SECCM study of gas bubble nucleation on silica nanoparticles. AFM images were collected on a Bruker Multimode 8 atomic force microscope in the air by tapping mode. The silicon cantilevers used here were purchased from Bruker with a spring constant of 20−80 N/m. The images were collected with a scan rate of 1 Hz and a scanning density of 512 lines/frame

Glass micropipettes characterization

Single channel micropipettes with different tip opening radii were obtained by pulling from borosilicate glass capillary (1.0 mm O.D., 0.55 mm I.D.) using a Sutter P-1000 puller. Fig. S3 shows the fabricated glass pipette with a tip opening radius of 1.5 µm.

Scan rate independence of cyclic voltammetries

Fig. S4 shows the voltammetric study of single bubble nucleation on both the bare glassy carbon surface and a 50 nm-radius SiO_2 nanoparticle. Voltammograms are independence of scan rates over the range from 0.1 to 2.0 V/s, suggesting the fast mass transport and bubble nucleation kinetics.

Stochasticity of single bubble nucleation

Fig. S5 summarizes the statistics and histograms of i_b^p distribution from 50 independent measurements at a single spot on the bare glassy carbon surface and on a 50 nm-radius SiO_2 nanoparticle. It is found that bubble nucleation for both cases shows excellent reproducibility and the single peak Gaussian distribution of i_b^p suggests the stochastic nature of bubble nucleation.

Dependence of single bubble nucleation on micropipette-substrate distance

In the SECCM configuration, a portion of the H_2 generated within the microdroplet is anticipated to diffuse to the microdroplet surface and escape into the surrounding air. We explored this possibility by recording bubble formation behavior with the pipette tip positioned at different heights above the substrate. After the electrolyte solution droplet initially contacted the glassy carbon substrate surface (defined as $\Delta d = 0$), voltammograms were recorded as the pipet was further moved towards the substrate surface. Fig. S6 shows the bubble nucleation peak current, i_b^p, from peak-shaped voltammograms are essentially the same within a distance range from 0 to 300 nm for a 1.5 µm-radius tip opening pipette. This result suggests that the electrolyte liquid from the pipette has a stable droplet in contact with the glassy carbon surface during the SECCM measurement.

Single bubble nucleation measurement using a galvanostatic method

Fig. S7 present a galvanostatic measurement of single H_2 bubble nucleation in SECCM. On the bare glassy carbon surface, the cyclic voltammetry shows a critical nucleation current, i_b^p, at −

179.3 nA (Fig. S7a). When the electrode is stepped from 0 nA to different currents from −170.0, −178.0, −179.0 to −180.0 nA, respectively, it is observed that higher currents of −179.0 and −180.0 nA result in the bubble nucleation, as evidenced by a further rapid increase in potential. Analogously, on a 50 nm-radius SiO_2 nanoparticle, the cyclic voltammetry shows a critical nucleation current, i_b^p, at −94.2 nA (Fig. S7c). When the electrode is stepped from 0 nA to different currents from −90.0, −92.0, −94.0 to −95.0 nA, it is observed that a higher current of −94.0 and −95.0 nA result in the bubble nucleation. Therefore, the bubble nucleation peak current, i_b^p, from cyclic voltammetry is very close to the intrinsic critical current for bubble nucleation.

SECCM mapping of single bubble nucleation on bare GC surface

Fig. S8 presents the SECCM mapping of single bubble nucleation across the bare GC surface. It is found that each position shows consistent bubble formation and there is slight spatial nonuniformities in nucleation current across the smooth GC surface.

SECCM mapping of single bubble nucleation on a 50 nm-radius SiO₂

Fig. S9 presents the same correlated SEM images and SECCM mapping as Fig. 2 in the main text, but with electrochemical and structural information for additional spots. Fig. S9c shows for two separated nanoparticles at spot IV, the critical i_b^p decreases to −82.18 nA and for three connected nanoparticles at spot VI, the critical i_b^p decreases to −89.38 nA. Individual voltammograms for each spot is presented in Fig. S10.

Fig. S11 presents an additional correlated SEM and SECCM mapping from single bubble nucleation measurements on 50 nm-radius SiO_2 nanoparticles. When a single 50 nm-radius SiO_2 nanoparticle is incorporated within a droplet at spots I , II and III, the critical i_b^p decreases significantly to −118.5, 101.1 and −116.2 nA, respectively. A two-connected and three-connected 50 nm-radius SiO_2 nanoparticles at spots IV and V leads to a critical i_b^p of −95.5 and −103.1 nA, respectively.

SECCM mapping of single bubble nucleation on a 99, 37 and 25 nm-radius SiO₂

Fig. S13 presents a typical correlated SEM images and SECCM mapping study of single H_2 bubble nucleation on glassy carbon surface with single 99 nm-radius SiO_2 nanoparticles. When a single 99 nm-radius SiO_2 nanoparticle is incorporated within a droplet at spot I, II, III, IV and V, the bubble nucleation current i_b^p decreases to −125.9, −144.5, −139.3, −143.9 and −137.6 nA, respectively. When two separated 99 nm-radius SiO_2 nanoparticles are incorporated within a droplet at spot VI, the critical i_b^p changes to −135.7 nA. When one isolated and two connected 99 nm-radius SiO_2 nanoparticles are encapsulated at spot VII, the critical i_b^p decreases to −126.9 nA. Individual voltammograms for each spot is presented in Fig. S14.

Fig. S15 presents a typical correlated SEM images and SECCM mapping study of single H_2 bubble nucleation on glassy carbon surface with single 37 nm-radius SiO_2 nanoparticles. When a single 37 nm-radius SiO_2 nanoparticle is incorporated within a droplet at spot I, II and III, the bubble nucleation current i_b^p decreases to −89.35, −85.01 and −83.08 nA, respectively. When one isolated and two connected 37 nm-radius SiO_2 nanoparticles are encapsulated at spot IV, the critical i_b^p decreases to −88.43 nA. When two connected and three connected 37 nm-radius SiO_2 nanoparticles are encapsulated at spot V, the critical i_b^p decreases to −88.55 nA. When two connected 37 nm-radius SiO_2 nanoparticles are encapsulated at spot VI, the critical i_b^p decreases to −79.66 nA. Individual voltammograms for each spot is presented in Fig. S16.

Fig. S17 presents a typical correlated SEM images and SECCM mapping study of single H_2 bubble nucleation on glassy carbon surface with single 25 nm-radius SiO_2 nanoparticles. When a single 25 nm-radius SiO_2 nanoparticle is incorporated within a droplet at spot I, II, III and IV, the bubble nucleation current i_b^p decreases to –68.32, –60.02, –77.26 and –65.03 nA, respectively. When two connected 25 nm-radius SiO_2 nanoparticles are encapsulated at spot V, the critical i_b^p decreases to –72.13 nA. Individual voltammograms for each spot is presented in Fig. S18.

Possible contamination from air after SECCM

In some cases (such as Fig. S15), co-located SEM shows the presence of particles within the microdroplet, while bubble nucleation on a nanoparticle is not considered. Close scrutiny of SEM image shows the seemly particles are actually not the SiO_2 nanoparticles (in terms of dimension and contrast), but more likely contaminations by the air after SECCM measurement. Locations with such feature is not considered for the single bubble nucleation analysis in Fig.3.

Liquid contact angle measurement on bare GC, SiO₂ nanoparticle films and quartz

The macroscopic contact angle of 10 µL droplets of H_2SO_4 on different surfaces without potential bias was measured by an optical contact angle goniometer with automatic dispenser (Attension Theta Lite Tensiometer). The profile of the droplet was recorded using a video camera and the stable contact angle measured at about 10 seconds after droplet contact was adopted. Fig. S20 shows that pre-cleaned glassy carbon surface has a contact angle of 91°, while hydrophilic SiO_2 exhibit smaller contact angle of 71°-77°, depending on different radius and the pre-cleaned flat quartz surface has a contact of 55°-35°.

Finite element simulation of local H₂ concentration

The H_2 gas concentration distribution near the electrode in SECCM is estimated from finite element simulation using the Transport of Diluted Species module within COMSOL Multiphysics 5.6. We used a meniscus geometry similar to Unwin's work(1) and the 2D axial symmetric geometry is shown in Fig. S21. The contact angle (θ) of 91° measured from liquid droplet is adopted to describe the contact angle of electrode/liquid/air interface in the SECCM. In the simulations, the pipet tip opening radius is set to be 1.5 µm. Distance between the pipette ending and substrate is assumed as 1.0 µm. The diffusion coefficient of H_2 and H^+ in the 2.0 M H_2SO_4 aqueous solution is set to 2.5 $\times10^{-5}$, and 5.0 $\times10^{-5}$ cm²/s (2, 3). Standard rate constant (k^0) for proton reduction on the glassy carbon is set to 5 $\times10^{-4}$ cm/s. Transfer coefficient in B-V kinetics (α) is set to 0.5. Gas transfer rate constant (k^{gas}) is set to 0.1 cm/s. Boundary conditions are summarized in Table S1. Fig. S22 indicates that the highest H_2 concentration always occurs at the particle/electrode interface, irrelevant to the position where particle is located within the droplet. Fig. S23 shows the simulated steady-state H_2 concentration profile within the droplet with corresponding SiO_2 nanoparticle radii and bubble nucleation peak current. Fig. S24 shows that the concentration of dissolved H_2 at the electrode is highest at the center of the electrode within the droplet, and decreases dramatically along the direction towards the liquid/air interface.

Theoretical calculation of free energy of bubble nucleation on a nanoparticle

A model of bubble nucleation is illustrated in Fig. 4a. As indicated in the figure, a bubble nucleus in a shape of ring, with two principal radii, r_1 and r_2, can be nucleated around the SiO_2 nanosphere of radius R on the GC substrate. The hydrophilicity of the SiO_2 nanosphere and that of the GC surface are denoted by their corresponding Young's contact angles, θ_1 and θ_2. The contact area between the nucleus and the nanosphere can be determined by the filling angle as θ_0 (Fig. 6a). Three potential pathways for bubble nucleation can be identified, depending on the level of gas supersaturation, particle size and nanosphere surface hydrophobicity: i) when the bubble nucleus is of a smaller size compared to the particle, i.e., $\theta_0 \leq \theta_1$, it nucleates strictly inside the crevice; ii) when the nucleus has a comparable size as the nanosphere, which leads to $\theta_1 < \theta_0 < \theta_1 + 90°$, it nucleates from the crevice but shows a shape that moves out of the mouth of the crevice; iii) when

the nucleus is substantially larger than the particles, $\theta_0 \geq 180°$, the critical nucleus completely wraps the particles as shown in Fig. S25.

We assumed that only the dissolved gas, H_2, in the bubble nucleus, and the change in the free energy for the bubble generation, ΔG, can be determined by(4),

$$\Delta G = -\Delta PV + N(\mu_b - \mu_l) + \sum \gamma A \tag{S1}$$

where V is the volume of the bubble, N is the number of gas molecules in the bubble, γ is the interfacial tension, A represents interfacial area, and μ is the chemical potential. The subscripts 'b' and 'l', represent the bubble and the liquid solution respectively. The pressure difference between the inside and outside of the nucleus, $\Delta P = P_b - P_l = P_b - P_0$, can be determined by Laplace equation $\Delta P = 2\gamma(1/r_1 + 1/r_2)$, with r_1, r_2 the two principal radii of curvature.

The chemical potential difference between gas in the bubble and the dissolved gas in the solution can be determined by

$$\Delta \mu = \mu_b - \mu_l = kT \ln\left(\frac{P_b}{P_0}\right) - kT \ln S \tag{S2}$$

with k the Boltzmann's constant, T the ambient temperature, P_0 the ambient pressure, and S the relative saturation nearby the electrode surface. In the nucleation process, we assume that the generated gas molecules enrich around the glassy carbon surface, leading to a large, local gas supersaturation $S = C^*/C^s$. Due to steady-state electrochemical generation of H_2 gas within the meniscus droplet, the local concentration of the gas near the GC surface, C^*, can be estimated by the Faradaic current, i,(5)

$$i = 4\pi nFDC^* r_p \left(\frac{1 - \cos \theta_p}{2 \tan \theta_p}\right) \tag{S3}$$

with n the number of electrons transferred per molecule of H_2 generated, F the Faraday's constant, D the diffusion coefficient for H_2, r_p the pore radius at the opening of the pipette, θ_p the half angle of the pipette.

The change in the interface free energy during bubble nucleus growing consists of three parts,

$$\sum \gamma A = (\gamma_{s1} - \gamma_{ls1})A_1 + (\gamma_{s2} - \gamma_{ls2})A_2 + \gamma_l A_3 = \gamma_l (A_1 \cos \theta_1 + A_2 \cos \theta_2 + A_3) \tag{S4}$$

where the subscripts '1', '2' and '3', denote the nanosphere, the GC substrate and the nucleus respectively. γ_{s1}, γ_{ls1} and γ_{s2}, γ_{ls2} are the gas-solid interfacial tension and liquid- solid interfacial tension on the side of the nanosphere and the substrate, respectively, γ_l is the gas-liquid interfacial tension of the bubble, and θ is the Young contact angle. In eq S4 Young' equation $\cos \theta = (\gamma_s - \gamma_{sl})/\gamma_l$ was used.

Depending on the nucleation path chosen, the bubble geometry can be described with

$$r_1 = r, \ r_2 \approx \begin{cases} r + R\sin \theta_0 - r\sin(\theta_1 - \theta_0) & \text{Path I, Path II} \\ r & \text{Path III} \end{cases} \tag{S5}$$

$$A_1 = \begin{cases} 2\pi R^2 (1 - \cos \theta_0) & \text{Path I, Path II} \\ 4\pi R^2 & \text{Path III} \end{cases} \tag{S6}$$

$$A_2 = \begin{cases} \pi \{R\sin \theta_0 + r[\sin \theta_2 - \sin(\theta_1 - \theta_0)]\}^2 & \text{Path I} \\ \pi \{R\sin \theta_0 + r[\sin \theta_2 + \sin(\theta_0 - \theta_1)]\}^2 & \text{Path II} \\ \pi r^2 \sin^2 \theta_2 & \text{Path III} \end{cases} \tag{S7}$$

$$A_3 = \begin{cases} 2\pi R r\left(1-\cos\theta_0\right)+2\pi r\left(\pi-\theta_1-\theta_2+\theta_0\right)\left[R\sin\theta_0-r\sin\left(\theta_1-\theta_0\right)\right] & \text{Path I} \\ \begin{aligned} & 2\pi r\left[2r+2r\cos\theta_2-R\left(1-\cos\theta_0\right)\right] \\ & +2\pi r\left(\pi-\theta_1-\theta_2+\theta_0\right)\left[R\sin\theta_0-r\sin\left(\theta_1-\theta_0\right)\right] \end{aligned} & \text{Path II} \\ 2\pi r^2\left(1+\cos\theta_2\right) & \text{Path III} \end{cases}$$

(S8)

$$V = \begin{cases} f_1\left(R,\theta_0,\theta_1,\theta_2\right) & \text{Path I} \\ f_2\left(R,\theta_0,\theta_1,\theta_2\right) & \text{Path II} \\ \dfrac{1}{3}\pi r^2\left(1+\cos\theta_2\right)^2\left[3r-r\left(1+\cos\theta_2\right)\right]-\dfrac{4}{3}\pi R^2 & \text{Path III} \end{cases}$$

(S9)

The bubble volumes from path I and path II, f_1 and f_2, are of complicated form, and they can be determined numerically. Inserting eqs S2-S9 into eq S1 and setting $d\left(\Delta G\right)/dN=0$, the maximal free energy difference is identified as the nucleation barrier for the bubble formation, ΔG^* (Fig. 4b). At a given gas supersaturation, the bubble nucleation barrier is found to vary with the nanoparticle radius (Fig. 4c). Consistent with the experimental observations, the barrier first decreases with the nanoparticle size until a minimal is reached, after which it then increases with particle size. The appearance of the minimum value of the nucleation barrier comes from the competition between various contributions of free energy change, as shown in Fig. S26.

As indicated in Fig. S26a, for large particles (e.g., $R > 20$ nm), bubble nucleation follows the path I (Fig. 4c). In this particular path, it is the gas-SiO$_2$ interfacial free energy that dominates the energy barrier for bubble nucleation (Fig. S26a). The figure shows that as R increases, the corresponding contact area between gas and the SiO$_2$, A_1, increases and its contribution to free energy change ($\gamma_l A_1 \cos\theta_1$) increases, leading to an increase in the nucleation barrier. For small particles ($R < 10$ nm), however, the bubble nucleation is achieved through path II or III (Fig. S26b). In this case, it is the contribution of the gas-liquid interface that dominates the nucleation: as R increases, A_3 decreases, resulting in a decrease in the interfacial free energy as well as in the nucleation barrier.

In general, particle size affects not only the shape of the bubble nucleus, but also the nucleation path. This is because the dominant term of nucleation barrier would change with particle size. When the size of nanospherical particle increases from rather small particle size, the dominant factor for bubble nucleation gradually changes from the contribution of gas-liquid interface to that for the gas-SiO$_2$ interface, resulting in the appearance of the minimum nucleation barrier under the certain particle size. Further increasing the nanosphere size leads to the increase of the nucleation barrier gradually.

The hydrophilicity of SiO$_2$ and that of GC substrate also affect the bubble nucleation. We changed the Young's contact angle from 50° to 55° and that for GC surface from 91° to 99° (within the range of possible deviations of experimental measurements). The corresponding nucleation barriers are given in Fig. S27 as a function of nanosphere size. In Table S3, we also summarize the determined particle size at which the minimal nucleation barrier appears. In general, within the range of parameters we explored, hydrophilicity of the two solid surfaces certainly affects the required nucleation barrier as well as the critical nanosphere size with the minimal nucleation barrier, but the overall effect is insignificant.
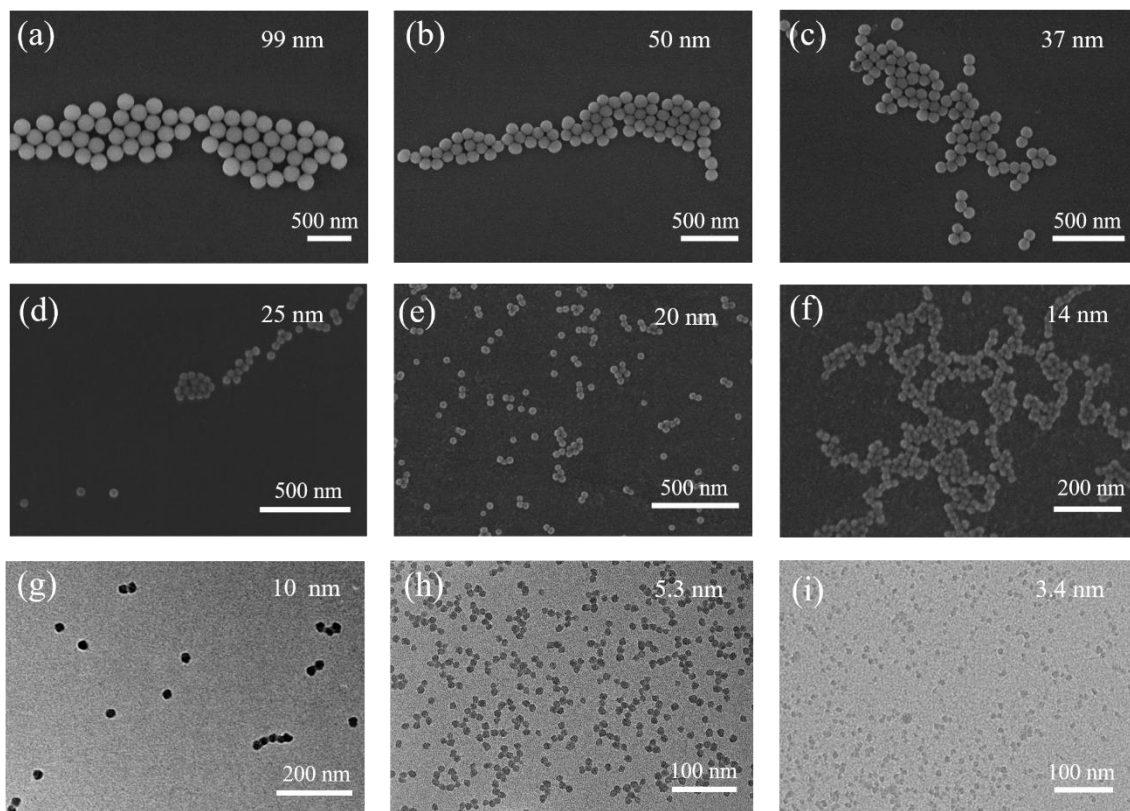
Fig. S1. SEM and TEM images of as-prepared SiO$_2$ nanoparticles with radius of (a) 99 ± 2 nm, (b) 50 ± 2 nm, (c) 37 ± 2 nm, (d) 25 ± 1 nm, (e) 20 ± 1 nm, (f) 14 ± 1 nm, (g) 10 ± 0.8 nm, (h) 5.3 ± 0.8 nm and (i) 3.4 ± 1.0 nm.
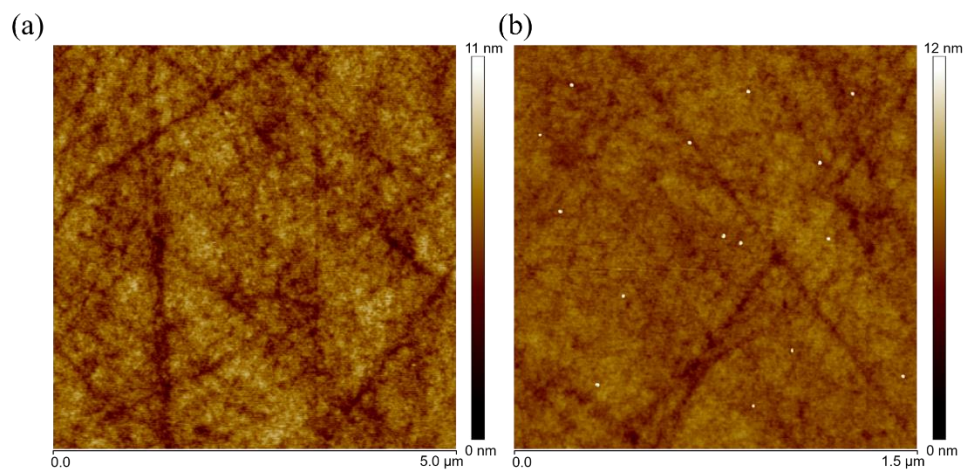
Fig. S2. Tapping mode AFM height images of a (a) polished glassy carbon surface and (b) glassy carbon surface deposited with individual 5.3 nm-radius silica nanoparticles.
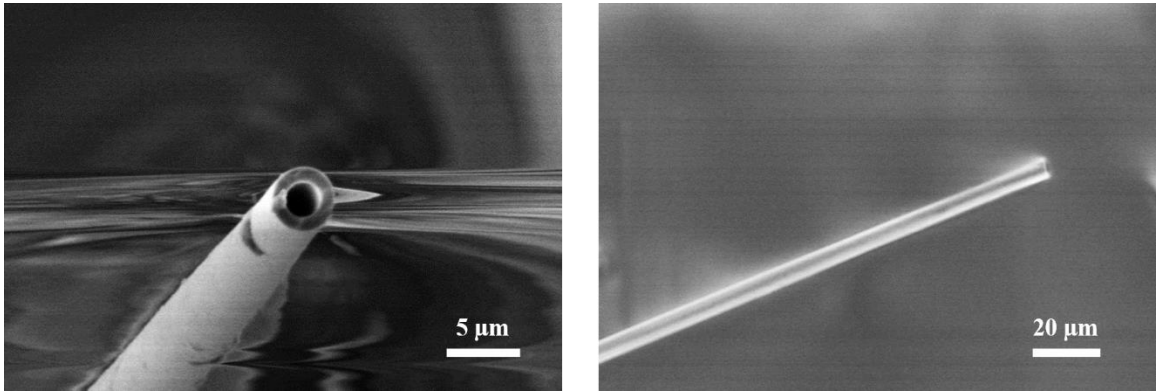
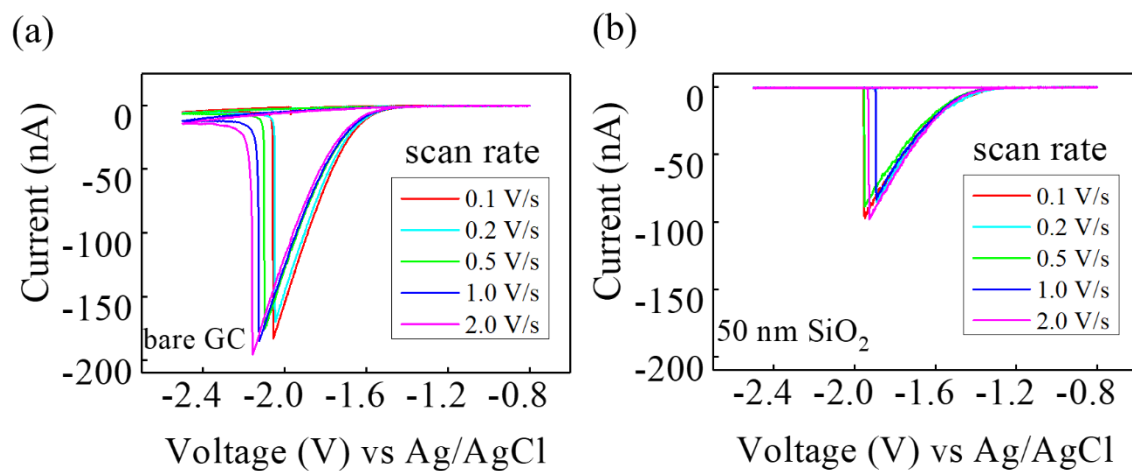**Fig. S3.** SEM images of a glass pipette with tip opening radius of 1.5 µm.

(a) (b)

Fig. S4. Cyclic voltammetries for HER and H_2 bubble formation at different scan rates on (a) bare glassy carbon and (b) a 50 nm-radius SiO_2 nanoparticle in SECCM using 2.0 M H_2SO_4 solution as the electrolyte.
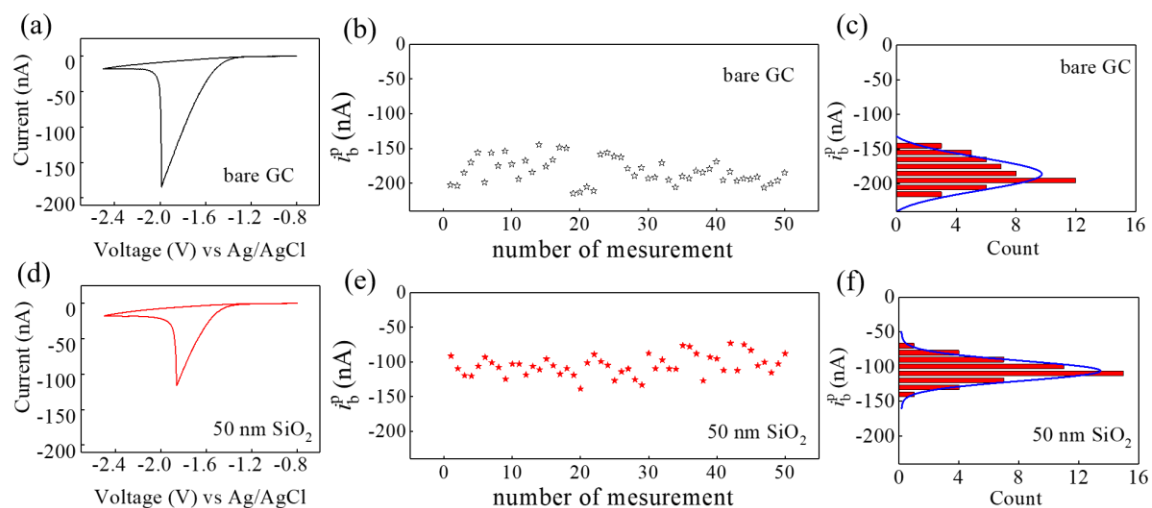
Fig. S5. (a, d) Typical cyclic voltammetry; (b, e) H_2 bubble nucleation peak currents, i_b^p, as a function of independent measurement number; (c, f) histograms of i_b^p distribution for single H_2 bubble nucleation on (a, b, and c) bare glassy carbon surface and (d, e, and f) a 50 nm-radius SiO_2 nanoparticle. In experiment, a 1.5 µm-radius pipette and 2.0 M H_2SO_4 solution was used at scan rate of 0.5 V/s.
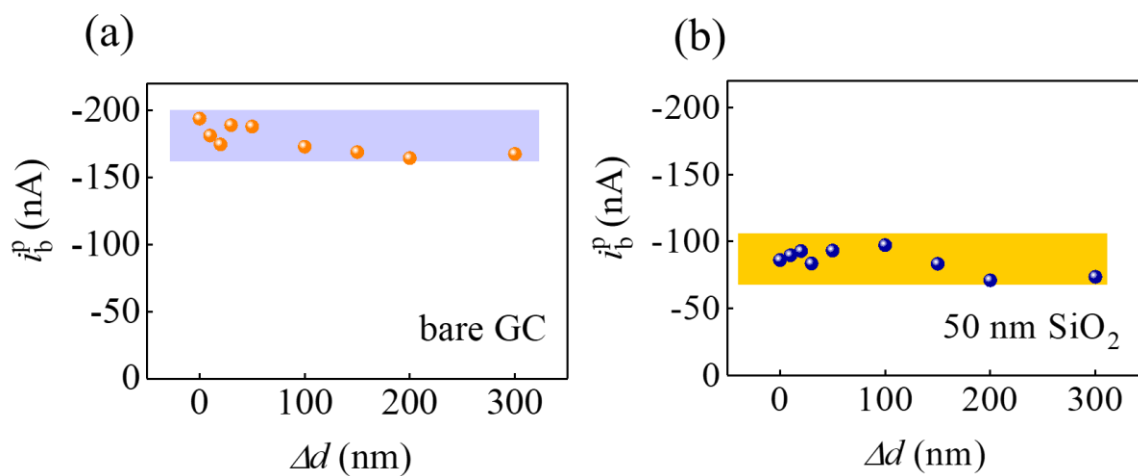
Fig. S6. The bubble nucleation peak current, i_b^p, from peak-shaped voltammograms of single bubble nucleation as a function of micropipette-substrate distance on (a) the bare glassy carbon surface, (b) a 50 nm-radius SiO_2 nanoparticle. Note, Δd is defined as 0 when the meniscus droplet first contacts the electrode surface, as indicated by the electric current signal.
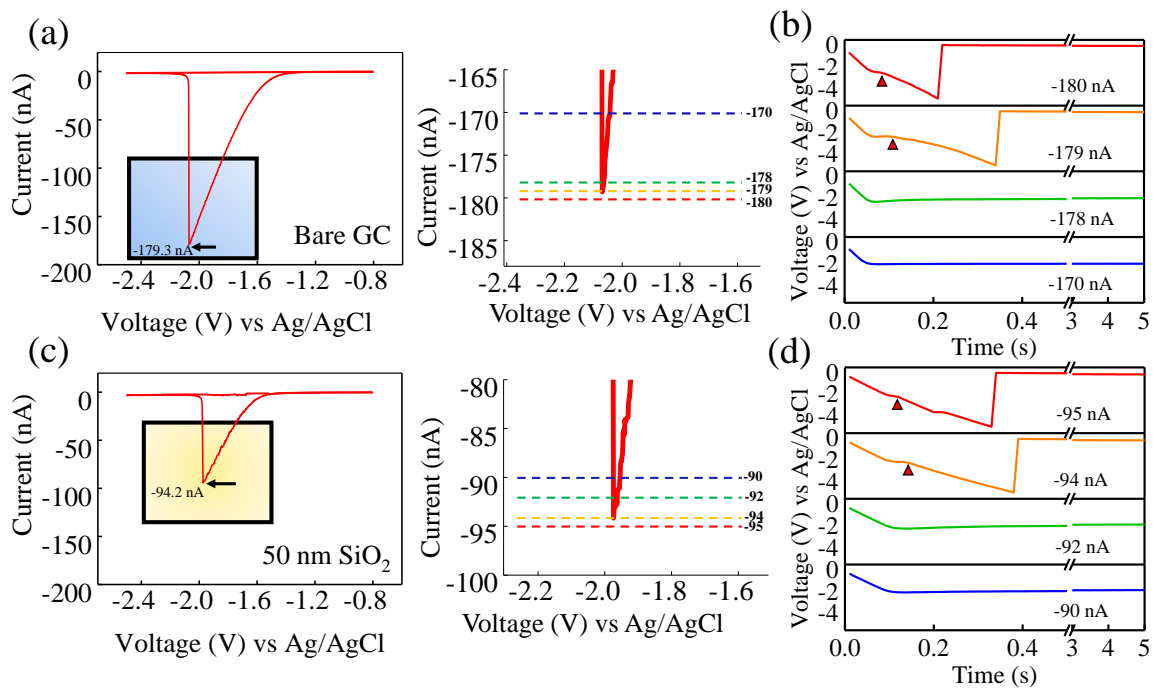
Fig. S7. Nucleation of a H_2 gas bubble in SECCM as measured using cyclic voltammetry on (a) a flat bare glassy carbon and (c) a 50 nm-radius SiO_2 nanoparticle at 0.5 V/s, and a galvanostatic method (b) on a flat glassy carbon with current stepped from 0 nA to −170, −178, −179 and −180 nA, and (d) on a 50 nm-radius SiO_2 nanoparticle with current stepped from 0 nA to −90, −92, −94 and −95 nA. The nucleation of a single H_2 bubble is indicated by a rapid increase in the potential at noted by the red triangles. When the potential becomes higher than the set threshold (−5 V), the current applied is returned to 0 nA.

13
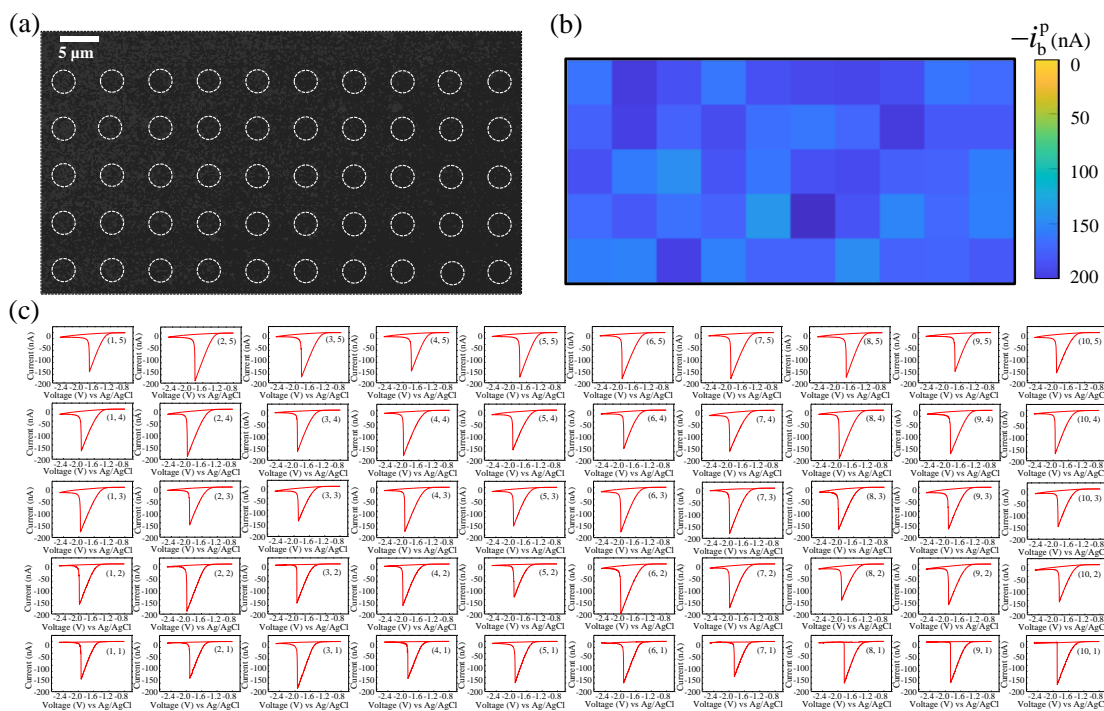
Fig. S8. (a) SEM image of bare glassy carbon surface; (b) SECCM mapping of bubble nucleation peak current i_b^p across the surface; (c) corresponding voltammograms for individual spots with location as labeled. In the SECCM experiment, a 1.5 μm-radius pipette filled with 2.0 M H_2SO_4 aqueous solution was used. Voltammograms were recorded at 0.5 V/s with a step size of 7 μm.
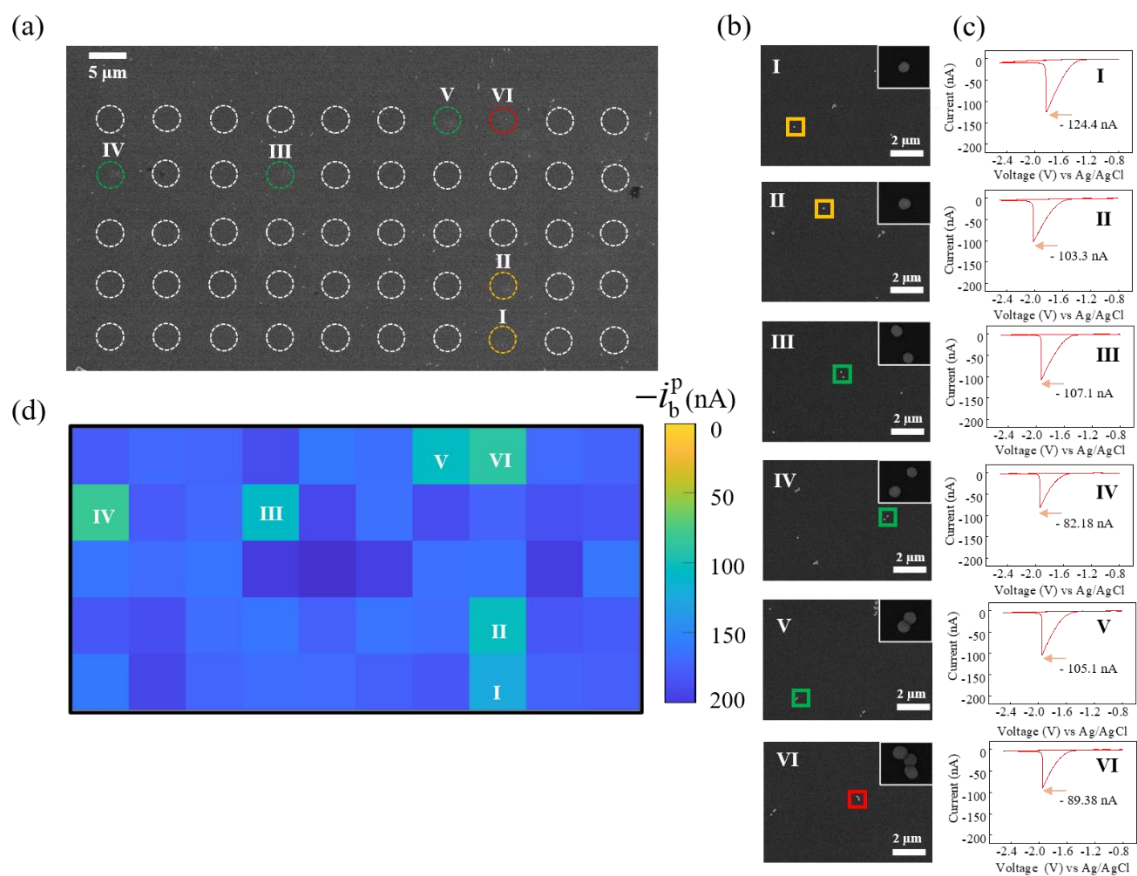
Fig. S9. Correlated (a) SEM image and SECCM mapping identical to Fig. 2 in the main text. Additional separated two nanoparticles or three connected nanoparticles with corresponding voltammograms are illustrated.
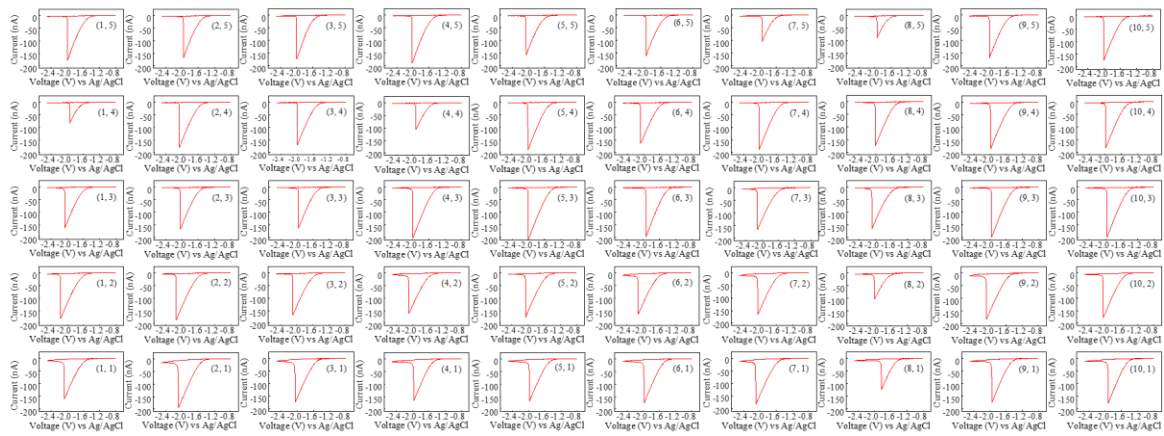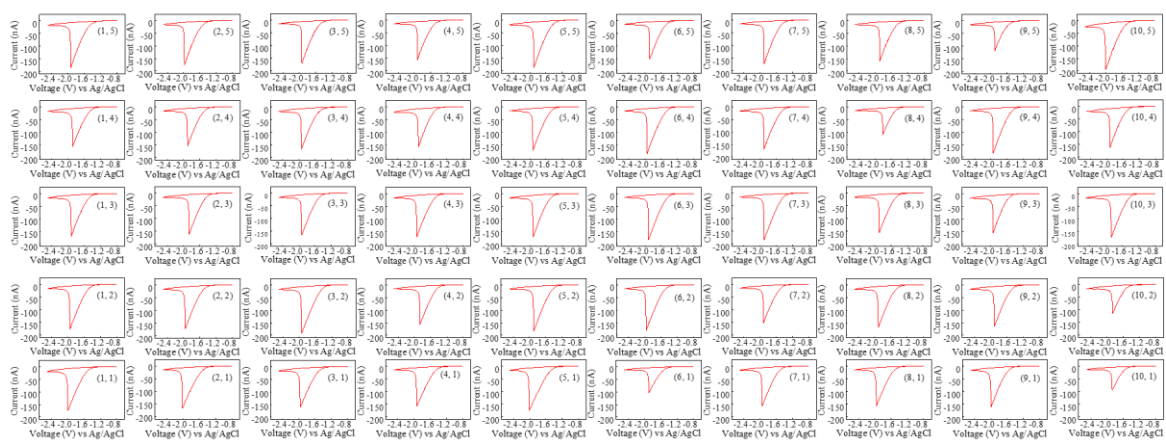
Fig. S10. Cyclic voltammetries corresponding to Fig. 2 measured for 5 × 10 spots in the SECCM study on glassy carbon surface immobilized with single 50 nm-radius SiO_2 nanoparticles.
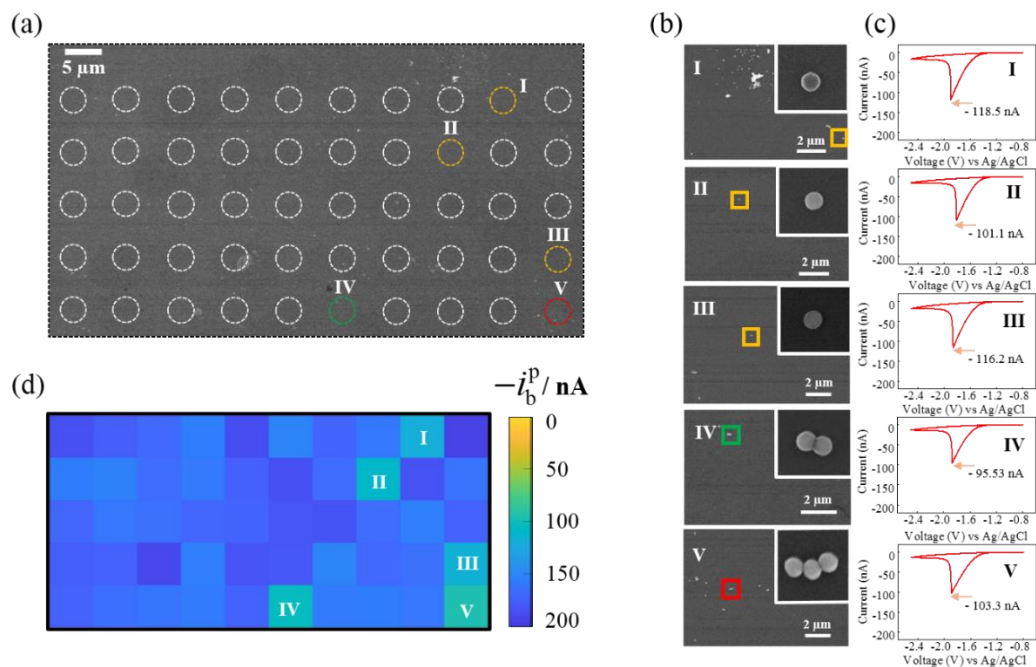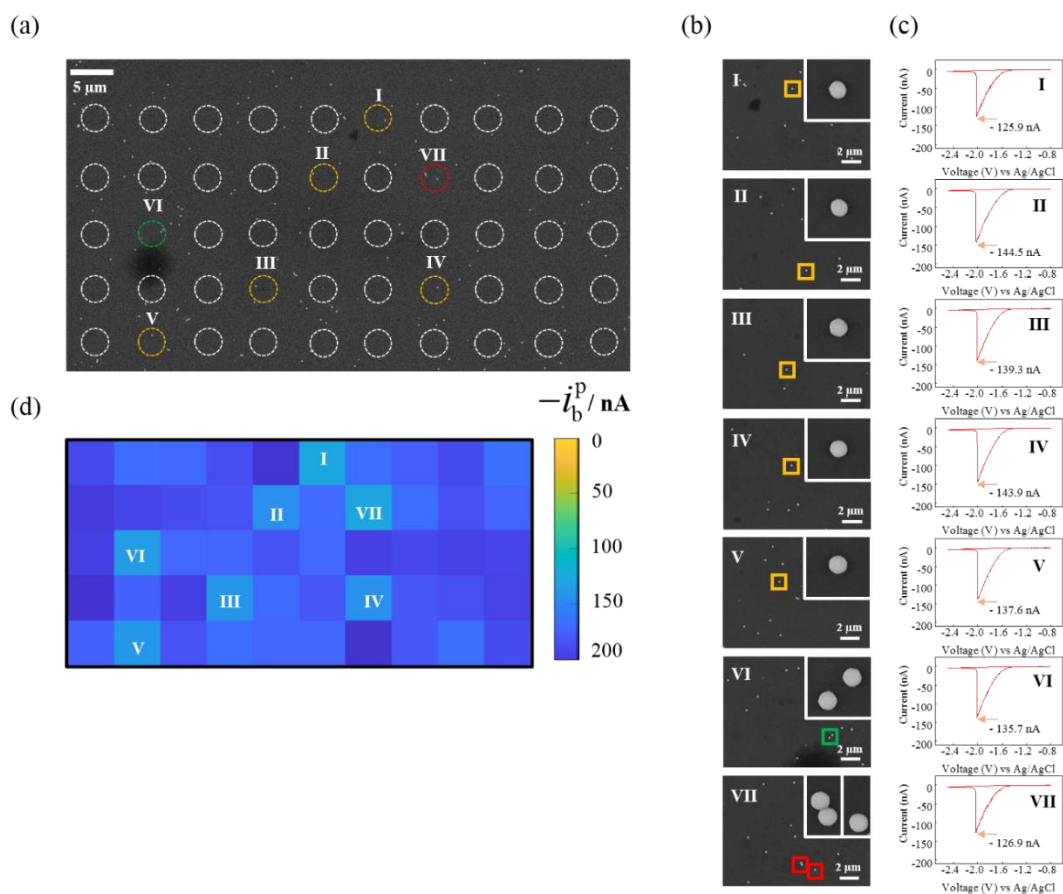
Fig. S11. (a) SEM image of the glassy carbon surface with well dispersed 50 nm-radius SiO_2 nanoparticles; (b) Zoom-in SEM images of partial locations with SiO_2 nanoparticles; (c) corresponding voltammograms for spots in (b); (d) SECCM images of bubble nucleation peak current i_b^p across the surface in (a). The insets in b are the corresponding magnified SEM images of individual SiO_2 nanoparticles. In the SECCM experiment, a 1.5 µm-radius pipette filled with 2.0 M H_2SO_4 aqueous solution was used. Voltammograms were recorded at 0.5 V/s with a step size of 7 µm.
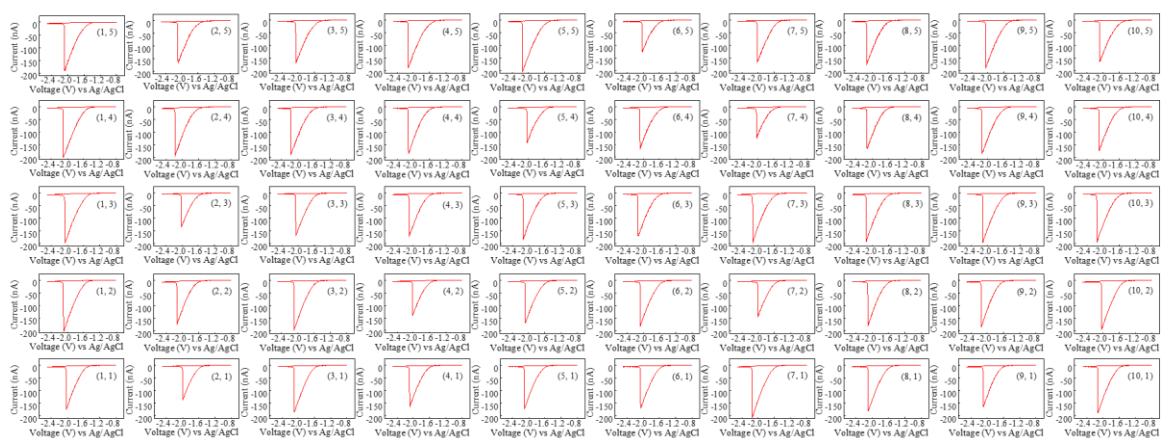
Fig. S12. Cyclic voltammetries corresponding to Fig. S12 measured for 5 × 10 spots in the SECCM study on glassy carbon surface immobilized with single 50 nm-radius SiO$_2$ nanoparticles.
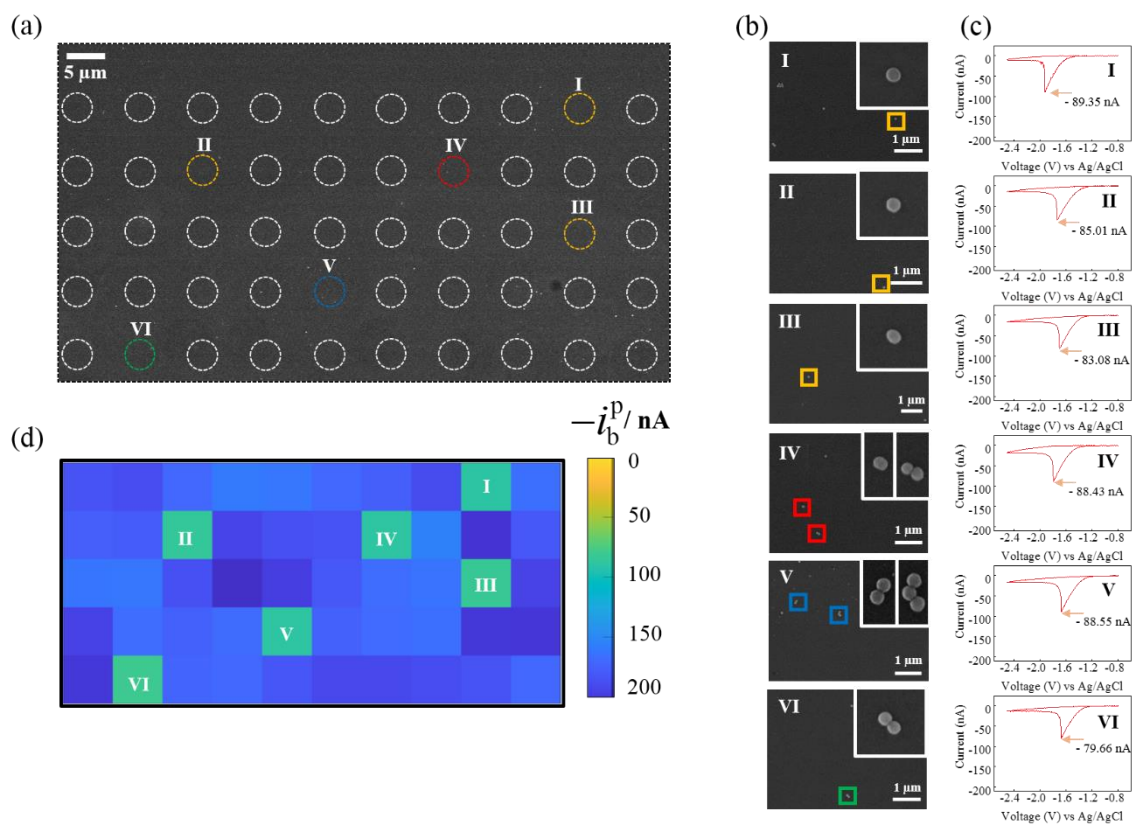
Fig. S13. (a) SEM image of the glassy carbon surface with well dispersed 99 nm-radius SiO_2 nanoparticles; (b) Zoom-in SEM images of partial locations with SiO_2 nanoparticles; (c) corresponding voltammograms for spots in (b); (d) SECCM images of bubble nucleation peak current i_b^p across the surface in (a). The insets in b are the corresponding magnified SEM images of individual SiO_2 nanoparticles. In the SECCM experiment, a 1.5 μm-radius pipette filled with 2.0 M H_2SO_4 aqueous solution was used. Voltammograms were recorded at 1.0 V/s with a step size of 7 μm.

Fig. S14. Cyclic voltammetries corresponding to Fig. S13 measured for 5 × 10 spots in the SECCM study on glassy carbon surface immobilized with single 99 nm-radius SiO_2 nanoparticles.

Fig. S15. (a) SEM image of the glassy carbon surface with well dispersed 37 nm-radius SiO_2 nanoparticles; (b) Zoom-in SEM images of partial locations with SiO_2 nanoparticles; (c) corresponding voltammograms for spots in (b); (d) SECCM images of bubble nucleation peak current i_b^p across the surface in (a). The insets in b are the corresponding magnified SEM images of individual SiO_2 nanoparticles. In the SECCM experiment, a 1.5 μm-radius pipette filled with 2.0 M H_2SO_4 aqueous solution was used. Voltammograms were recorded at 1.0 V/s with a step size of 7 μm.
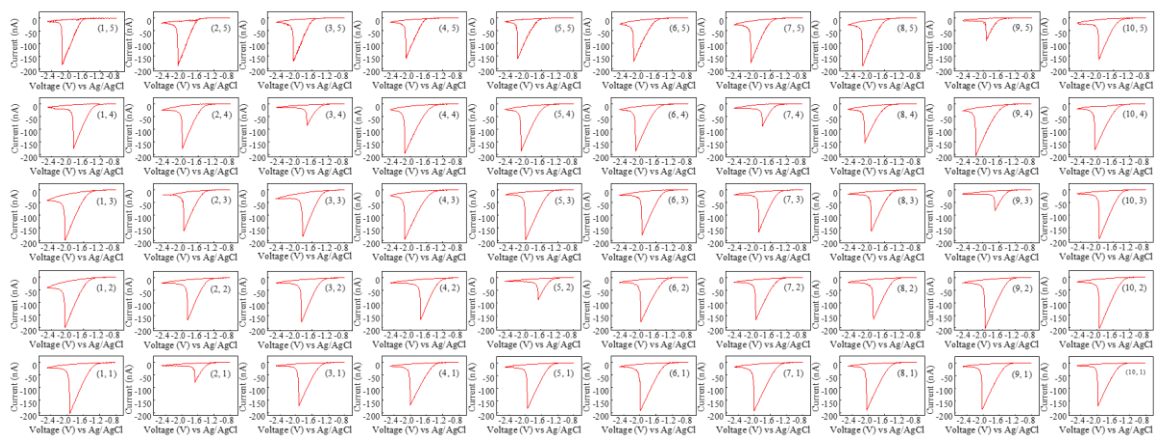
Fig. S16. Cyclic voltammetries corresponding to Fig. S15 measured for 5 × 10 spots in the SECCM study on glassy carbon surface immobilized with single 37 nm-radius SiO_2 nanoparticles.
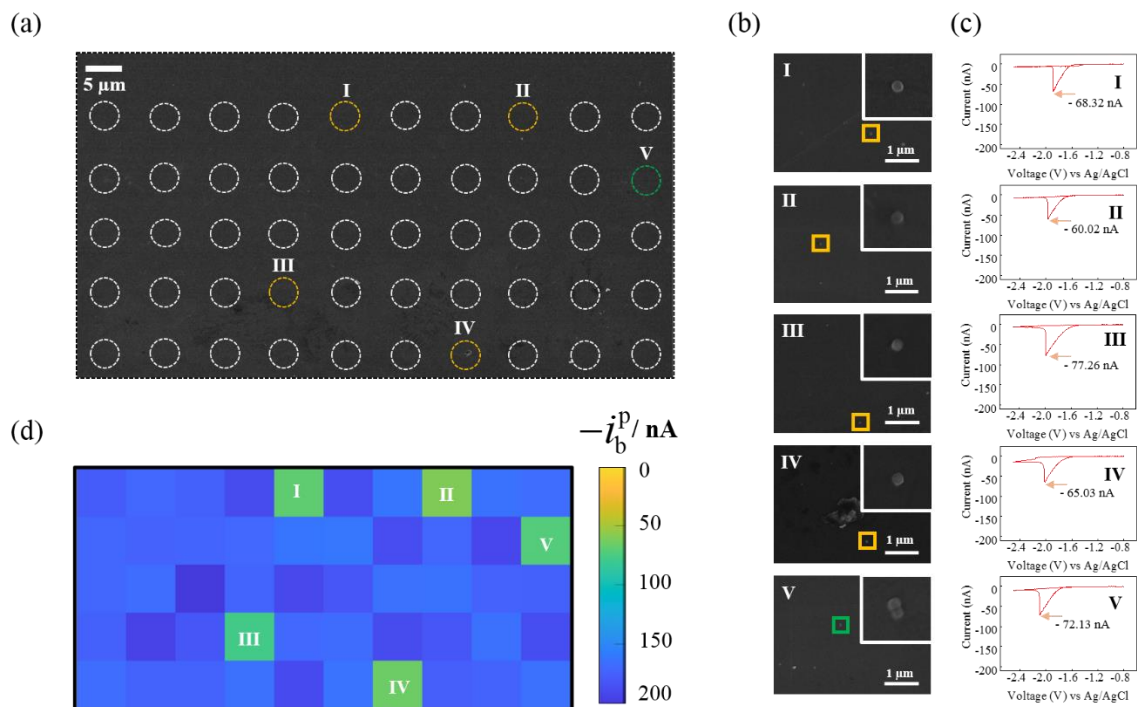
Fig. S17. (a) SEM image of the glassy carbon surface with well dispersed 25 nm-radius SiO_2 nanoparticles; (b) Zoom-in SEM images of partial locations with SiO_2 nanoparticles; (c) corresponding voltammograms for spots in (b); (d) SECCM images of bubble nucleation peak current i_b^p across the surface in (a). The insets in b are the corresponding magnified SEM images of individual SiO_2 nanoparticles. In the SECCM experiment, a 1.5 μm-radius pipette filled with 2.0 M H_2SO_4 aqueous solution was used. Voltammograms were recorded at 1.0 V/s with a step size of 7 μm.
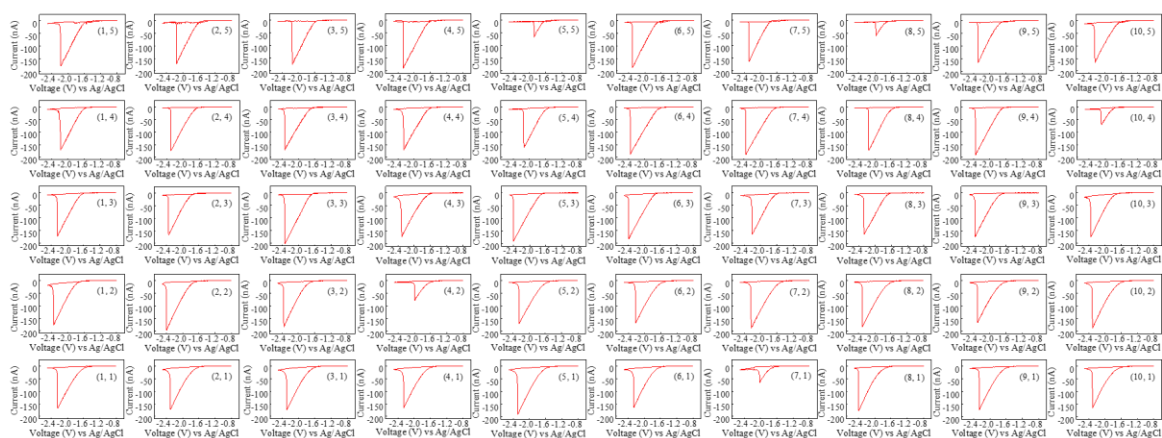
Fig. S18. Cyclic voltammetries corresponding to Fig. S17 measured for 5 × 10 spots in the SECCM study on glassy carbon surface immobilized with single 25 nm-radius SiO_2 nanoparticles.
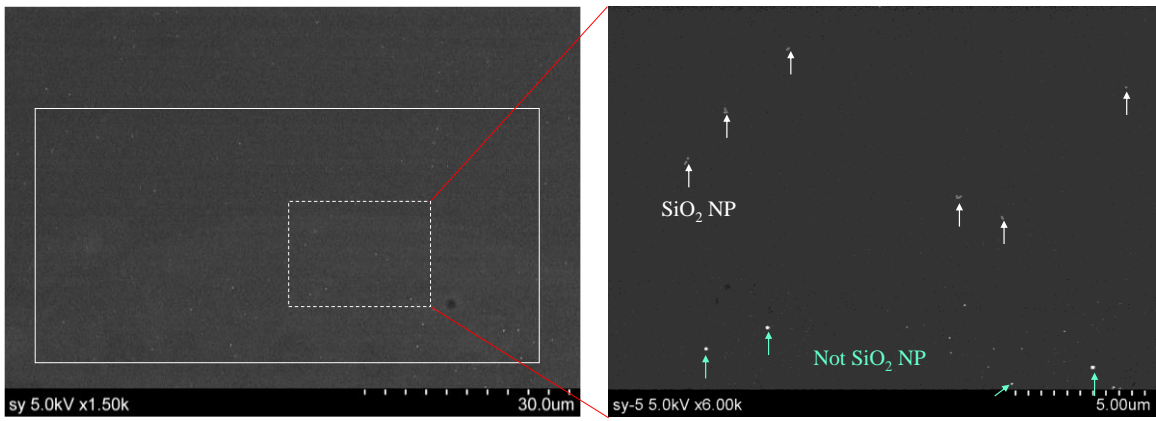
Fig. S19. SEM images for the SiO$_2$ nanoparticle deposited glassy carbon surface, examined after SECCM mapping. Although observed very occasionally, there are situations where particles on the surfaces are not the SiO$_2$ nanoparticles. Bubble nucleation study at the position is not counted for quantitative analysis.
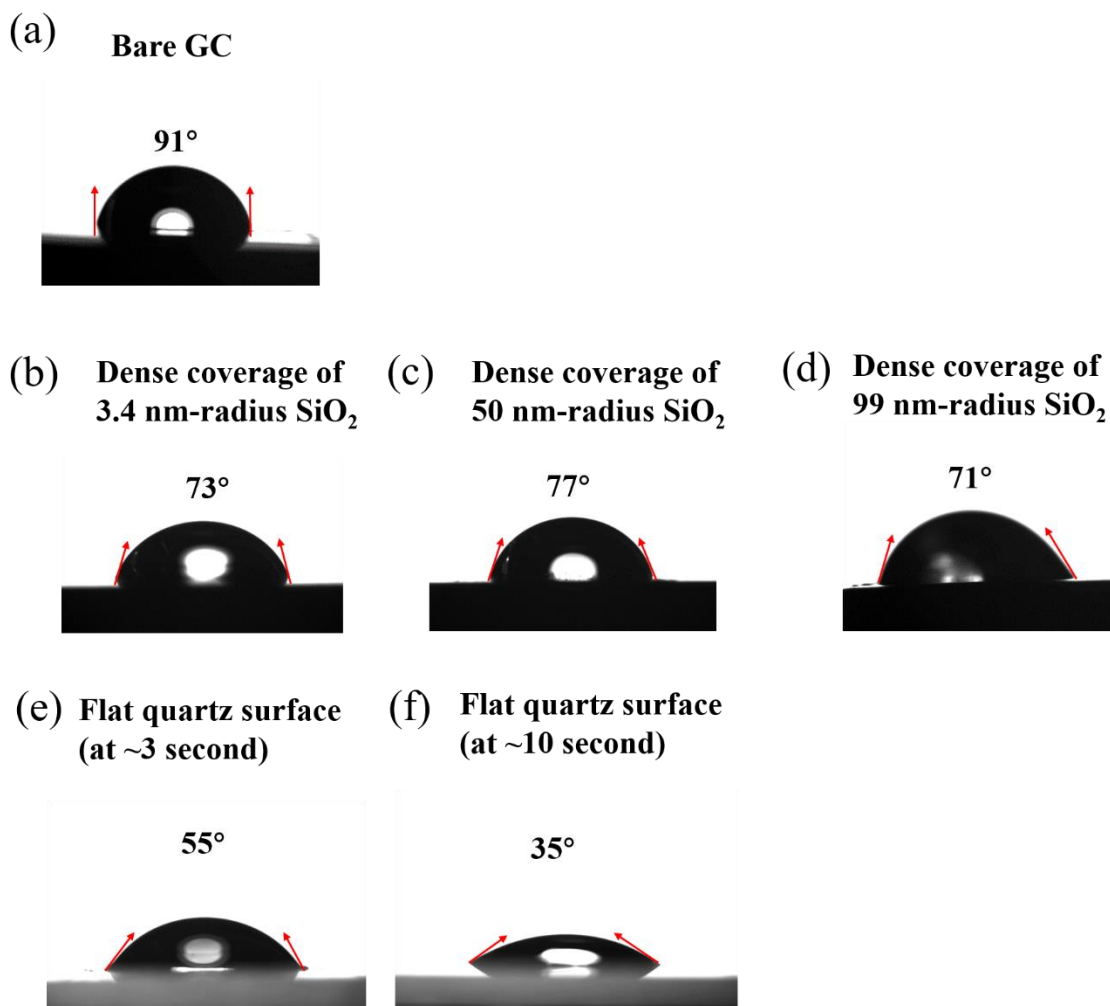
(a) **Bare GC**

91°

(b) **Dense coverage of 3.4 nm-radius SiO$_2$**

73°

(c) **Dense coverage of 50 nm-radius SiO$_2$**

77°

(d) **Dense coverage of 99 nm-radius SiO$_2$**

71°

(e) **Flat quartz surface (at ~3 second)**

55°

(f) **Flat quartz surface (at ~10 second)**

35°

Fig. S20. Droplet contact angles of 2.0 M H$_2$SO$_4$ solution on (a) bare GC, (b) 3.4 nm-radius SiO$_2$ film, (c) 50 nm-radius SiO$_2$ film, (d) 99 nm-radius SiO$_2$ film, (e) flat quartz surface at the time of ~3 second), and (f) flat quart surface at the time of ~10 second. A 10 μL liquid droplet was used in the contact angle measurement and the angle was measured based on the images took at a time of ~10 second after droplet contact was formed.
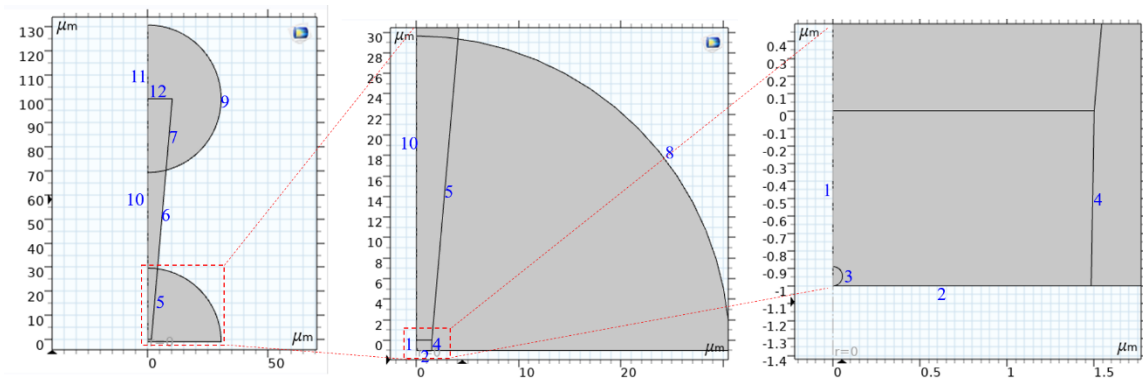
Fig. S21. Geometry of the finite element model with labeling of all the boundaries for simulating the SECCM experiment. The pipette tip opening radius is set to be 1.5 μm and the distance between the pipette ending to the electrode surface is set to be 1.0 μm.
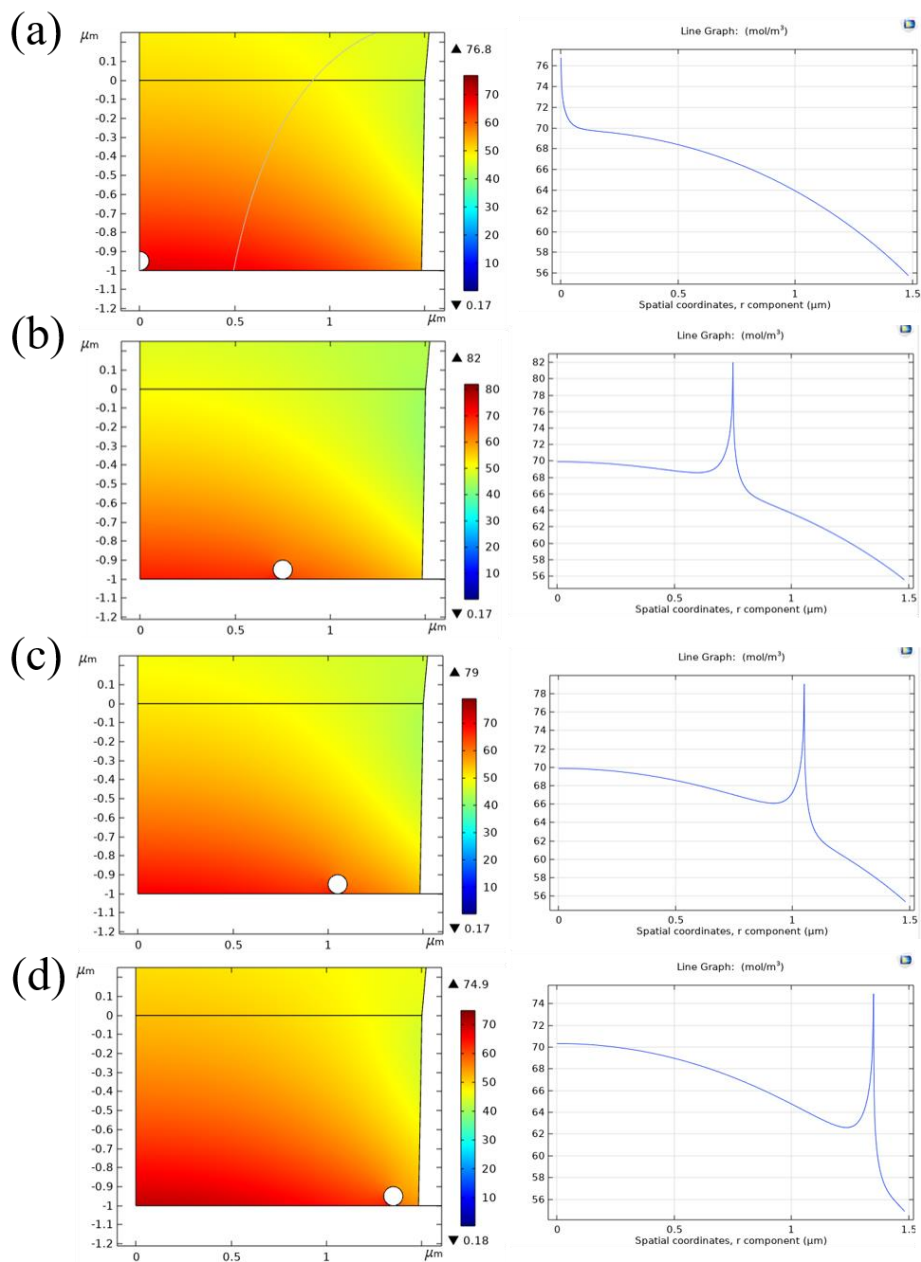
Fig. S22. Simulated steady-state H_2 concentration profile within the droplet with a 50 nm radius SiO_2 nanoparticle sitting (a) in the center of the droplet and (b) $0.5r_{pipette}$; (c) $0.7r_{pipette}$; (d) $0.9r_{pipette}$ position along the radial within the droplet. The bottom panel presents that the surface H_2 concentration along the radial where it decreases gradually to the edge with the highest concentration occurring at the SiO_2 nanoparticle/electrode interface.
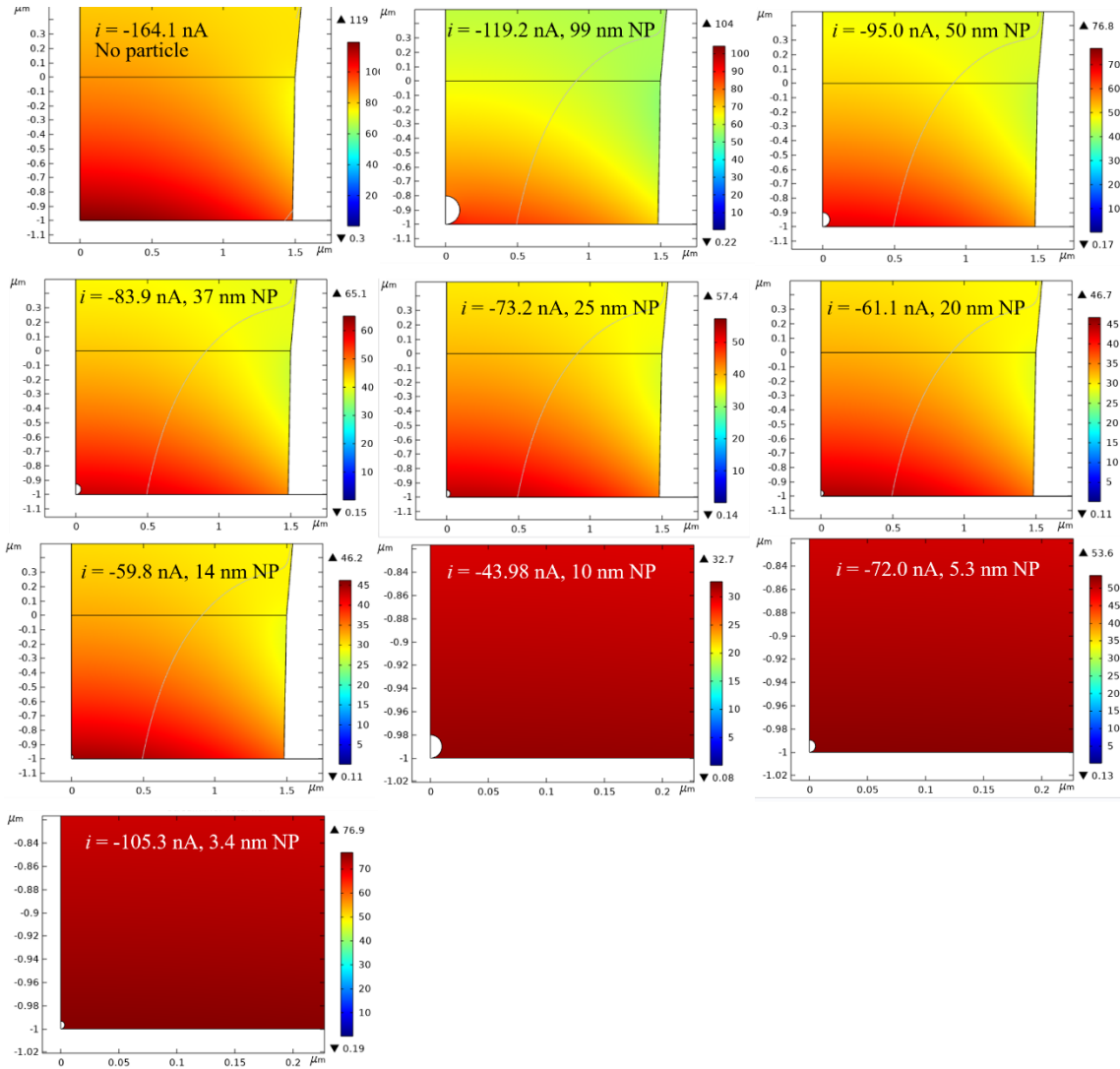
Fig. S23. Simulated steady-state H₂ concentration profile within the droplet with corresponding SiO₂ nanoparticle radii and bubble nucleation peak current, as indicated in the Figure, where D_{H_2} is set as 2.5×10^{-5} cm²/s,(3) H₂ gas transfer kinetic constant k^{gas} is set as 0.1 cm/s. Single nanoparticle is assumed to sit in the center of the droplet.
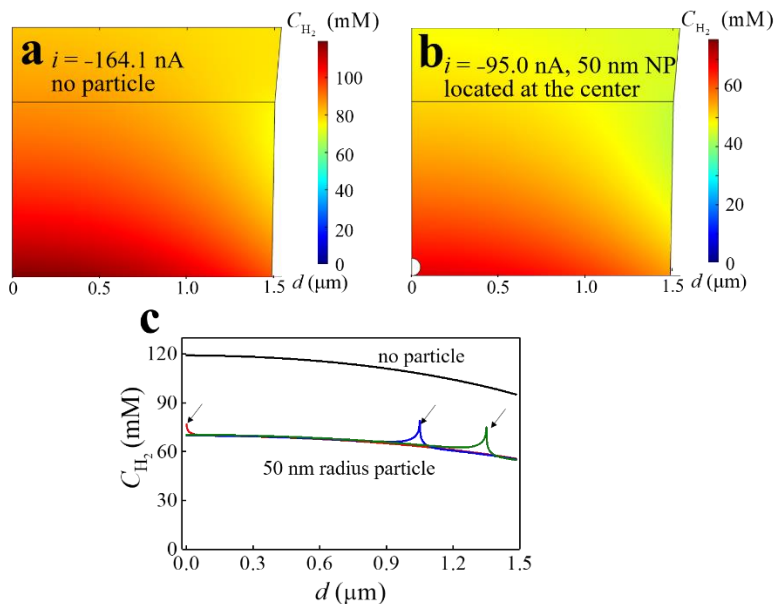
Fig. S24. Simulated local surface H$_2$ concentration profile inside the microdroplet (a) without a silica particle at −164.1 nA; (b) with a 50 nm-radius nanoparticle sitting in the center of the droplet at −95.0 nA; (c) H$_2$ concentration on electrode surface along the radial direction, where the highest value occurs at the SiO$_2$/electrode interface as indicated by the arrows. In the simulation, angle of the microdroplet is set as that of the macroscopic values, 91°, D_{H_2} in the 2.0 M H$_2$SO$_4$ aqueous solution is set as 2.5 × 10^{-5} cm^2/s (3) .
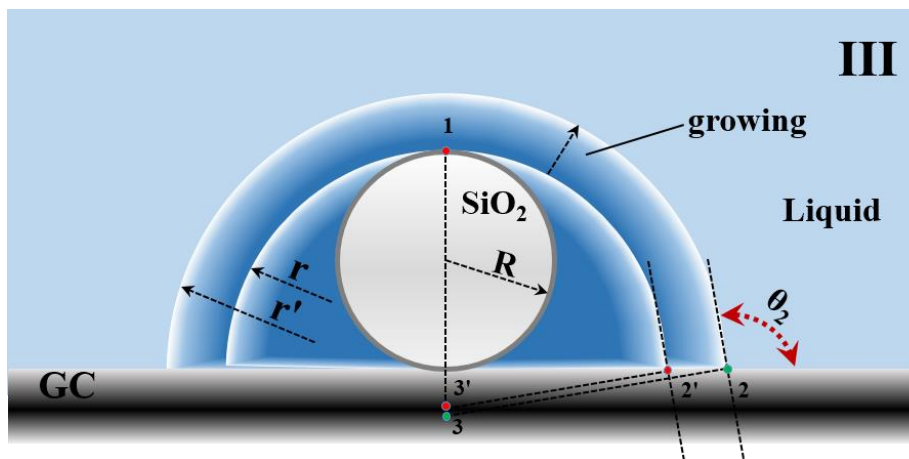
Fig. S25. Scheme of bubble nucleation and growth in the case the bubble nucleus is substantially larger than the SiO_2 nanosphere.
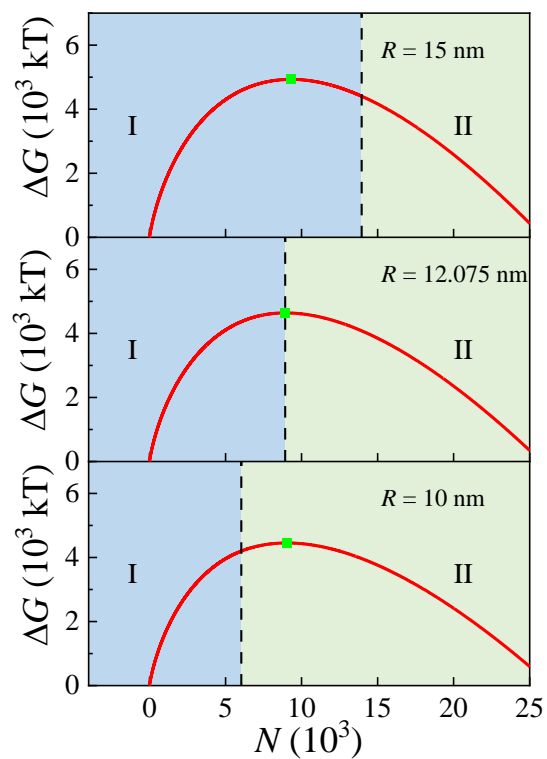
Fig. S26. Typical free-energy changes as a gas nucleus grows calculated from classic nucleation theory. The SiO$_2$ nanoparticle radius, R, is set as 15, 12.075 and 10 nm and the solution supersaturation, ζ, is set as 150. $\theta_1 = 55°$ and $\theta_2 = 91°$. At $R = 15$ nm, the bubble nucleation occurs at regime **I**; At $R = 10$ nm, the bubble nucleation occurs at regime **II**; At $R = 12.075$ nm, the bubble nucleation free-energy reaches it maximum at the boundary of regime **I** and **II**.
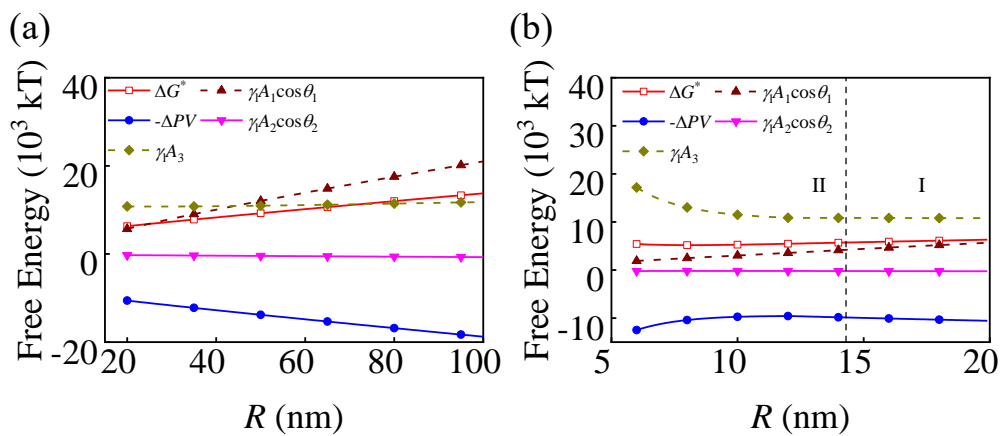
Fig. S27. Various contributions for the nucleation barrier and as a function of the size of SiO_2 nanosphere at a fixed gas supersaturation of 150 ($\theta_1 = 55°$, $\theta_2 = 91°$): (a) large nanosphere; (b) small nanosphere.
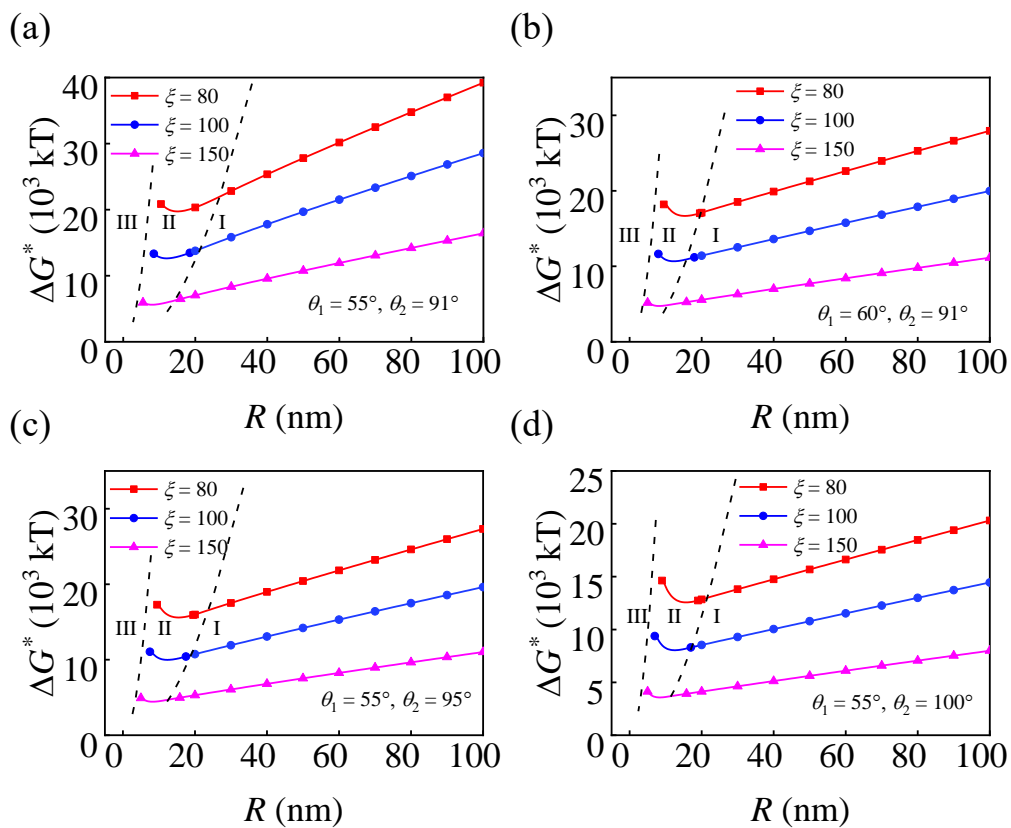
Fig. S28. The relationship between the nucleation energy barrier and the size of SiO_2 nanosphere. In this figure, we considered the effect of hydrophilicity of SiO_2 particle and the GC surface, as well as the effect of gas supersaturation. (a, b) $\theta_1 = 55°$ and $60°$ when θ_2 is fixed at $95°$. (c, d) $\theta_2 = 95°$ and $100°$ when θ_1 is fixed at $55°$.
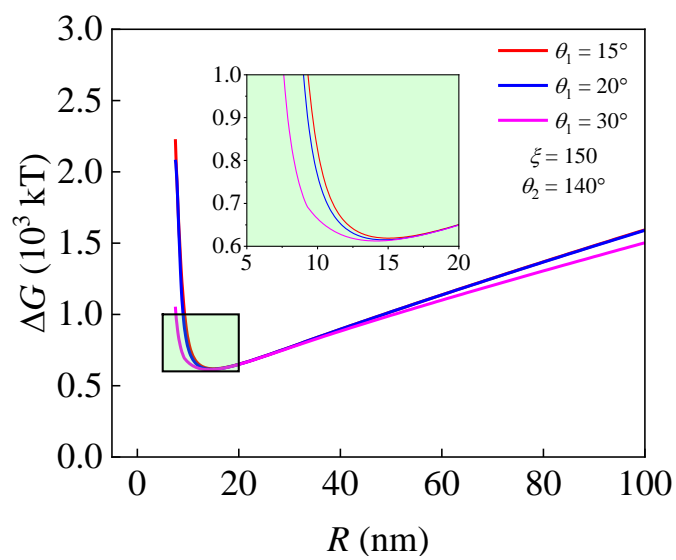
Fig. S29. Overall free-energy barrier for bubble nucleation as a function of SiO_2 nanoparticle radius at assumed bubble contact angle ($\theta_1 = 15, 20, 30°$, and $\theta_2 = 140°$) and supersaturation ($\zeta = 150$).

Table S1. Boundary conditions used in the finite element model..

Boundary	Boundary conditions
1, 10, 11	2D axial symmetry
2	Electrode surface: $i = \text{intop}(flux_{\text{H}^+})*\text{Faraday constant}$ $flux_{\text{H}^+} = -k^0 C_{\text{H}^+} e^{-\alpha f(E-E^0)} + 2k^0 C_{\text{H}_2} e^{(1-\alpha)f(E-E^0)}$
5	Constant bulk solution concentration
4,12	Gas exchange kinetics Solution side: $J_{\text{H}_2} = k^{\text{gas}}*(C_{\text{H}_2}^{\text{air}}/K - C_{\text{H}_2}^{\text{aq}})$ Air side: $J_{\text{H}_2} = -k^{\text{gas}}*(C_{\text{H}_2}^{\text{air}}/K - C_{\text{H}_2}^{\text{aq}})$
3, 5, 6 ,7	No flux
8, 9	Constant bulk gas concentration

Table S2. Physical parameters used in this work.

parameter	
P_0 (kPa)	101.325
T (K)	298.15
γ_l (N/m)	0.065(6)
k (10^{-23} J/K)	1.38
F (C/mol)	96485
C^s (mM)	0.8
N	2
D (10^{-5} cm^2/s)	2.5(3)
r_p (μm)	1.5
θ_p (°)	5

Table S3. The determined minimum nucleation barrier, ΔG_{min}^{*} and the corresponding size of SiO_2 nanosphere.

θ_1 (°)	θ_2 (°)	ξ					
		80		100		150	
		R (nm)	ΔG_{min}^{*} (10^3 kT)	R (nm)	ΔG_{min}^{*} (10^3 kT)	R (nm)	ΔG_{min}^{*} (10^3 kT)
50	91	15.1	19.74	12.0	12.63	8.0	5.61
55	91	15.2	18.20	12.2	11.65	8.1	5.18
	95	15.4	15.59	12.4	9.98	8.2	4.44
	100	15.7	12.57	12.5	8.04	8.4	3.57
60	91	15.3	16.67	12.3	10.67	8.2	4.74

SI References

1.   Daviddi E*, et al.* Nanoscale visualization and multiscale electrochemical analysis of conductive polymer electrodes. *ACS Nano* 13:13271-13284.(2019)
2.   Barker AL & Unwin PR Measurement of solute partitioning across liquid/liquid interfaces using scanning electrochemical microscopy−double potential step chronoamperometry (secm−dpsc): Principles, theory, and application to ferrocenium ion transfer across the 1,2-dichloroethane/aqueous interface. *J. Phys. Chem. B* 105:12019-12031.(2001)
3.   Liu Y*, et al.* Visualization and quantification of electrochemical h2 bubble nucleation at pt, au, and mos2 substrates. *ACS Sens.* 6:355-363.(2021)
4.   Ward CA, Balakrishnan A, & Hooper FC On the thermodynamics of nucleation in weak gas-liquid solutions. *J. Basic Eng. Dec* 92:695-701.(1970)
5.   Hill JW & Hill CM Directly mapping photoelectrochemical behavior within individual transition metal dichalcogenide nanosheets. *Nano Lett.* 19:5710-5716.(2019)
6.   Jin C, Liu Y-L, Shan Y, & Chen Q Scanning electrochemical cell microscope study of individual h_2 gas bubble nucleation on platinum: Effect of surfactants. *Chinese J. Anal. Chem.* 49:e21055-e21064.(2021)